On the Splitting Methods of Inviscid Fluxes for Implementing High-Order Weighted Compact Nonlinear Schemes *

TU Guo-hua[1],　CHEN Jian-qiang[1,2],　MAO Mei-liang[1,2],

ZHAO Xiao-hui[1],　LIU Hua-yong[1]

(1. *State Key Laboratory of Aerodynamics*(*China Aerodynamics Research and Development Center*), *Mianyang*, *Sichuan* 621000, *P.R.China*;

2. *Computational Aerodynamics Institute*, *China Aerodynamics Research and Development Center*, *Mianyang*, *Sichuan* 621000, *P.R.China*)

Abstract:There is increasing popularity in using high-order weighted compact nonlinear schemes(WCNS) for complex flow simulations. The WCNS can be used in combination with many inviscid flux splitting methods. However, it is still uncertain which flux splitting is most suitable for the WCNS because most of the methods are devised on the basis of low-order discretization methods. It is also not very clear what will happen when these splitting methods are mounted directly in high-order accurate schemes. In order to provide some guide for selecting inviscid fluxes in the computation of surface heat transfer, the dissipations of the fluxes are studied. Every inviscid flux can be expressed as a summation of a central part and a dissipation part. All the fluxes have an identical central part which is very simple. However, different fluxes have different dissipation parts which are more or less complicated. The analysis on the source of flux dissipation shows that the dissipation is nearly proportional to flux jumps on grid interfaces. Numerical experiments show that high-order schemes usually produce far less flux jumps than low-order schemes in smooth regions, and logically the flux dissipations are quite lower. 3 canonical flows including hypersonic shock wave/boundary layer interactions(SWBLI) are simulated to show the influence of inviscid fluxes on heat transfer computing. Finally, a suggestion is given for selecting inviscid fluxes based on the dissipations and shock instabilities of van Leer's flux splitting, the Steger-Warming(SW) flux splitting, the kinetic flux vector splitting (KFVS), Roe's flux splitting, the AUSM(advection upwind splitting method)-type flux splitting and the HLL-type flux splitting.

Key words:WCNS; shock wave/boundary layer interaction; Euler flux; high-order accuracy; heat transfer rate

CLC number:　O35　　**Document code**:　A

doi:10.21656/1000-0887.370518

Introduction

Traditionally, 2nd-order accurate discretization schemes were widely used in applications of aerodynamics because of their simplicity, robustness and fast convergence. Recently, more and more people used high-order schemes for simulations and studies of turbulent flows, separated flows, shock wave/boundary layer interactions and computational aeroacoustics[1-2]. Compared to low-order schemes, high-order schemes are regarded as less robust and more complicated for understanding and coding. With the progress in computational fluid dynamics (CFD) within the last 10 years, the poor robustness of high-order finite difference methods (FDMs) was greatly improved in view of the latest achievements of geometric conservation law[3] and multi-block grid treatments[4-5]. Recent progresses[2,6-7] showed that some high-order schemes were also applicable on grids involving real aircraft/spacecraft configurations, which indicated that high-order schemes may also be suitable for solving engineering-oriented problems in CFD.

For high speed flows with shock waves, Pirozzoli[8] commented that the discretization schemes shall be accurate as well as low-dissipation in smooth flow regions, and simultaneously, these schemes shall capture shock waves stably and smoothly without obvious numerical oscillations. In the past 20 to 30 years, lots of studies have been done in pursuing these 2 conflicting goals, and many high-order schemes have been devised. Besides the weighted compact nonlinear schemes[9], there are many others high-order schemes like the discontinuous Galerkin schemes[10], the compact schemes with total variation diminishing[11-13], the weighted essentially non-oscillatory schemes[14], the spectral volume schemes[15] and the monotonicity preserving schemes[16]. The WCNS is highly valuable in solving a wide range of fluid problems, including incompressible, compressible and hypersonic flows, even on complex computational grids[2,4-5,17-18]. However, despite the achievements in high-order CFD, high speed flow simulations are still facing many challenges like numerical instabilities due to shock wave dominated strong nonlinear interactions including SWBLIs, shock/shock interactions, shock/shear layer interactions and shock/vortex interactions. The reliability of CFD is especially debatable for hypersonic flows in consideration of shock anomalies (such as numerical oscillations) and heating prediction capabilities[19].

Shock-capturing (or upwind) schemes usually need some kind of inviscid flux splitting methods to construct the fluxes at cell edges. Numerical oscillations, numerical dissipations and carbuncle phenomena were reported, more or less, related to the construction methods for inviscid fluxes. Kitamura et al.[19-22] made a wide range of investigations on the properties of several inviscid fluxes, but only based on low-order spatial schemes. Other than low-order schemes, Tu et al.[23] investigated the shock instability of quite a few inviscid fluxes by a 5th-order WCNS. Both Kitamura's results and Tu's results show that all the fluxes investigated in ref. [19-23] may lead to shock instabilities which will degrade the computation accuracy or even cause computation failures (such as negative pressure or density). Surface heating computations are usually deemed as tough tasks in CFD. Kitamu-

ra et al. suggested that, for hypersonic heating computations, inviscid flux functions should satisfy the following 3 conditions: (a) robustness and shock stability, (b) total enthalpy conservation, (c) resolution of boundary layer and temperature gradient. Unfortunately, no fluxes investigated by Kitamura et al. can concurrently satisfy all the 3 conditions. Kitamura et al.[22] reported that failure to satisfy either the 1st item or the 3rd one may lead to poor prediction of surface heating. Kitamura et al.[22] also reported that the lack of the 2nd item can be largely supplemented with 2nd-order schemes other than 1st-order schemes, while 2nd-order schemes were not enough to overcome the deficiency in all the 3 items, especially in the 3rd one. Up to now, it is still not known whether high-order discretization schemes can or can't compensate the shortcomings of inviscid fluxes. As there is increasing popularity of using high-order schemes, it is high time to investigate how much high-order spatial schemes can compensate for the deficiency of inviscid fluxes for hypersonic heating computations.

Many evidences (e.g. the tests in ref. [19]) show that other factors, such as limiters, spatial accuracy, reconstructed variables and aspect ratios of grids, do have as much or more impacts on numerical solutions than flux functions. Instead of studying all these factors, the present work only focus on the combination of the 5th-order spatial interpolation of the WCNS and inviscid flux constructions. Although there are many flux construction methods, they can be categorized into 2 splitting groups or some hybrid ones. The 2 groups are the flux vector splittings (FVSs) and the flux difference splittings (FDSs). The studies reported in literatures show that FDSs are usually less dissipative and likely to give sharper resolution for contact discontinuities compared with FVSs, but they are more likely to produce carbuncle phenomena. Users may feel puzzled when facing the problem of choosing a suitable inviscid flux for high-order schemes. In ref. [23], the 5th-order WCNS was applied to evaluate the shock instability of many inviscid fluxes, the shock instability therein showed much difference from that of low-order schemes. Because the left-to-right jumps of flow variables at cell edges where inviscid fluxes are constructed usually decrease with higher-order spatial reconstructions (or interpolations), Pandolfi and D'Ambrosio[24] claimed that carbuncle-like features are more evident in the plain 1st-order integration schemes than in more accurate reconstruction schemes. However, the investigation in ref. [23] indicates that this statement may not be true for shock instability. High-order schemes may be less likely to undergo visible carbuncle phenomena, but be more likely to encounter other shock instabilities such as numerical oscillations.

In order to provide some guide to choose suitable inviscid fluxes for high-order numerical schemes, this paper will further investigate the properties of inviscid fluxes in the computation of heat transfer, especially with the SWBLI.

1   Spatial schemes and flux splittings

1.1   Governing equations and spatial schemes

The time-dependent compressible Navier-Stokes/Euler equations are transformed in

curvilinear coordinates and expressed in a conservative form as

$$\frac{\partial \tilde{\boldsymbol{Q}}}{\partial \tau} + \frac{\partial \tilde{\boldsymbol{E}}}{\partial \xi} + \frac{\partial \tilde{\boldsymbol{F}}}{\partial \eta} + \frac{\partial \tilde{\boldsymbol{G}}}{\partial \zeta} = s \left(\frac{\partial \tilde{\boldsymbol{E}}_v}{\partial \xi} + \frac{\partial \tilde{\boldsymbol{F}}_v}{\partial \eta} + \frac{\partial \tilde{\boldsymbol{G}}_v}{\partial \zeta} \right), \tag{1}$$

where $\tilde{\boldsymbol{Q}} = \boldsymbol{Q}/J$, $\boldsymbol{Q} = [\rho, \rho u, \rho v, \rho w, \rho E]^{\mathrm{T}}$ are conservative variables, $\tilde{\boldsymbol{E}}$, $\tilde{\boldsymbol{F}}$, $\tilde{\boldsymbol{G}}$ are inviscid fluxes, and $\tilde{\boldsymbol{E}}_v$, $\tilde{\boldsymbol{F}}_v$, $\tilde{\boldsymbol{G}}_v$ are viscous fluxes, $s = 0$ for Euler equations and $s = 1$ for Navier-Stokes equations. Details of the equations are omitted here for they can be easily found elsewhere. For 1D or 2D problems, we only need to remove the corresponding unnecessary terms in eq.(1).

The inviscid (Euler) terms are discretized with the 5th-order WCNS (WCNS-E-5)[9]. Take the discretization of the invsicid term along the ξ direction as an example:

$$\frac{\partial \tilde{E}_i}{\partial \xi} = \frac{75}{64h} (\tilde{E}_{i+1/2} - \tilde{E}_{i-1/2}) - \frac{25}{384h} (\tilde{E}_{i+3/2} - \tilde{E}_{i-3/2}) + \frac{3}{640h} (\tilde{E}_{i+5/2} - \tilde{E}_{i-5/2}). \tag{2}$$

The inviscid fluxes at cell edges can be computed with an FVS or an FDS. The van Leer splitting[25], the Steger-Warming splitting[26] and the KFVS[27] are 3 typical FVSs. Roe's flux[28], the AUSM①[29-31] and the HLL[32-35] are 3 typical FDSs. All the fluxes can be written as

$$\tilde{E}_{i+1/2} = \tilde{E}(U^{\mathrm{L}}_{i+1/2}, U^{\mathrm{R}}_{i+1/2}), \tag{3}$$

where the flow variables $U^{\mathrm{L}}_{i+1/2}$ and $U^{\mathrm{R}}_{i+1/2}$ are located at cell edges, and can be computed with the various reconstruction or interpolation methods. In this paper, a 5th-order nonlinear weighted interpolation, a 2nd-order TVD scheme and a 1st-order scheme (upwind) are applied. The 5th-order interpolation can be found in ref. [9]. The 2nd-order TVD scheme is the non-oscillatory and non-free-parameter dissipative (NND) scheme[36]. The NND scheme is realized by setting $\partial \tilde{E}_i / \partial \xi = (\tilde{E}_{i+1/2} - \tilde{E}_{i-1/2})/\Delta \xi$, and the cell-edge flow variables are acquired by

$$\begin{cases} U^{\mathrm{L}}_{i+1/2} = U_i + \dfrac{1}{2} \operatorname{mmd}(U_{i+1} - U_i, U_i - U_{i-1}), \\[2mm] U^{\mathrm{R}}_{i+1/2} = U_{i+1} - \dfrac{1}{2} \operatorname{mmd}(U_{i+1} - U_i, U_{i+2} - U_{i+1}), \end{cases} \tag{4}$$

where "mmd" is a minmod limiter. The 1st-order upwind scheme is fulfilled by fixing mmd = 0.

The same discretization procedure is applied to the other directions of the curvilinear coordinate. The inviscid fluxes investigated below are listed in table 1. The entropy fix adopted in ref. [23] is also used in this paper.

The viscous terms are discretized with 2 different methods. The 1st method is a 2nd-order central scheme and is used in combination with the NND scheme or the 1st-order upwind scheme mentioned above. The 2nd method is a 6th-order one, and is used in combi-

---

① AUSM-type fluxes are sometimes deemed as a hybrid of an FDS and an FVS.

nation with the WCNS-E-5. For the 6th-order method, the cell-edge and cell-node staggered method of Tu et al.[37] is used.

The time discretization is performed with the 3rd-order TVD-type Runge-Kutta integration method[14] and the standard lower/upper symmetric Gauss-Seidel method for unsteady problems and steady problems, respectively.

Table 1　A list of the inviscid fluxes investigated

splitting type	FVS			
flux type	Steger-Warming		van Leer	KFVS
entropy fix or subtype	$\delta_{\text{fix}} = 0$	$\delta_{\text{fix}} = 0.1$	–	–

splitting type	FDS					
flux type	Roe		AUSM		HLL	
entropy fix or subtype	$\delta_{\text{fix}} = 0$	$\delta_{\text{fix}} = 0.1$	AUSMPW	AUSMPW+	HLLC p-based　HLLC Roe-based	HLLE

Note: (a) Entropy fix: $|\lambda_i^*| = \sqrt{\lambda_i^2 + \delta_{\text{fix}}^2 (\kappa_x^2 + \kappa_y^2)}$, where λ_i is the eigenvalue, $\kappa = \xi$ or η, and $\delta_{\text{fix}} = 0.1$.

(b) HLLC p-based: the wavespeed is estimated by the pressure correlation; HLLC Roe-based:

the wavespeed is estimated by Roe's average[35].

A proper algorithm for cell-edge metrics (such as $\tilde{\xi}_{x,i+1/2}$) is also very important for FDMs. All the metrics in this paper are acquired with the conservative metric method in ref. [38].

We would like to remind that, besides spatial accuracy orders and flux functions, many other factors such as limiters (if there are), viscous discretizations and grid allocations, all may have great influence on the stability and accuracy of numerical simulations. However, our main interest here is to find some guide to select inviscid flux for the 5th-order inviscid discretization, or more specifically, the WCNS-E-5. The 1st- and 2nd-order schemes herein are for readers' convenience of comparisons since many results of 1st- and 2nd-order methods can be easily found in the literatures.

1.2　Flux dissipations

No matter what kinds of flux splitting methods are used, a flux function may be expressed as the sum of a central part $\tilde{E}_C$ and a dissipation part $\tilde{E}_D$ as follows

$$\tilde{E}(U^L, U^R) = \tilde{E}_C + \tilde{E}_D. \tag{5}$$

The central part is quite simple and can be written as

$$\tilde{E}_C = \frac{\tilde{E}(U^L) + \tilde{E}(U^R)}{2}. \tag{6}$$

The dissipation part is more or less complicated and different flux functions produce different dissipations. An instructive expression for the dissipation can be written as

$$\tilde{E}_D \sim C(U^m) \Delta U, \tag{7}$$

where $\Delta U = |U^L - U^R|$ denotes the jumps between left-hand flow values and right-hand flow values at a cell interface; $C(U^m)$ is the coefficient for the dissipation, and is a function of U^m which denotes some intermediate flow values between U^L and U^R. The dissipation

is nearly [2] proportional to the flow jumps at a cell interface in smooth regions.

Take Roe's flux as the first example:

$$\widetilde{E}_{D}^{Roe} = -\frac{1}{2}\mid A^{Roe}\mid \Delta Q, \tag{8}$$

where $\Delta Q = Q^{R} - Q^{L}$ and $\mid A^{Roe}\mid = R^{Roe}\mid \Lambda^{Roe}\mid (R^{Roe})^{-1}$ is acquired by Roe's average of the left-side and right-side cell-edge flow variables. We can find from eq.(8) that

$$C(U^{m}) = -\mid A^{Roe}\mid /2.$$

The 2nd example is the Steger-Warming flux. Its dissipation part can be written as

$$\widetilde{E}_{D}^{SW} = -\frac{1}{2}\mid A^{L}\mid \Delta Q - \frac{1}{2}\Delta A Q^{R}, \tag{9}$$

where $\Delta A = \mid A(Q^{R})\mid - \mid A(Q^{L})\mid$ is the jump of the Jacobian matrix which is determined by the flow jumps. On the right-hand side of eq.(9), the 1st term is similar to the dissipation part of Roe's flux, while the 2nd term implies that the Steger-Warming flux is generally more dissipative than Roe's flux.

A more complex example is the advection upstream splitting method by pressure based weight functions (AUSMPW) [30] which is also regarded as a hybrid of an FVS and an FDS. As the AUSM-type fluxes split the inviscid flux vector into the so-called convection and pressure terms, and the 2 terms are reconstructed with different methods, then the dissipation terms of these fluxes are very complicated. Even though, the dissipation terms can also be written as functions nearly proportional to flow jumps.

The AUSMPW flux can be written as

$$\widetilde{E}^{AUSMPW} = \widetilde{E}_{C} + \widetilde{E}_{D}^{AUSMPW}, \tag{10}$$

here the central term is also eq.(6), while the dissipation term is much complex. We only consider the 1D case. Suppose

$$\Phi = [\rho, \rho u, \rho H]^{T}, \quad P = [0, p, 0]^{T}. \tag{11}$$

The dissipation is split into convection and pressure terms as

$$\widetilde{E}_{D}^{AUSMPW} = F_{D}^{\Phi} + F_{D}^{P}. \tag{12}$$

Then the dissipation terms can be written as follows

1) If $\mid Ma_{L,R}\mid = \dfrac{\mid u_{L,R}\mid}{c_{1/2}} \geqslant 1$,

$$F_{D}^{\Phi} = \begin{cases} \left[-\dfrac{u_{R}}{2} + \dfrac{u_{R} - \mid u_{R}\mid}{2}\omega \right]\Delta\Phi - \dfrac{\Phi_{L}}{2}\Delta\mid u\mid, & \text{if } m_{1/2} \geqslant 0, \\[4mm] \left[-\dfrac{u_{L}}{2} + \dfrac{u_{L} - \mid u_{L}\mid}{2}\omega \right]\Delta\Phi - \dfrac{\Phi_{R}}{2}\Delta\mid u\mid, & \text{else}, \end{cases} \tag{13}$$

---

② "nearly" here means "approximately" but also depends on the status of the left and the right sides. There is an example of exception: if U^{L} and U^{R} satisfy the Rankine-Hugoniot relations, the dissipation parts can reduce to 0, even though $\mid U^{R} - U^{L}\mid$ may be very large (e.g. crossing steady shock waves with large upstream Mach numbers). In smooth region, larger $\mid U^{R} - U^{L}\mid$ usually means more dissipation.

$$F_D^P = -\frac{P_L}{2}\Delta\mathrm{sign}(u) - \frac{\mathrm{sign}(u_R)}{2}\Delta P. \tag{14}$$

2) If $|Ma_{L,R}| = \dfrac{|u_{L,R}|}{c_{1/2}} < 1$,

$$F_D^{\Phi} = \begin{cases} -c_{1/2}\Phi_L\Delta Ma^{\beta-} + c_{1/2}Ma_R^-|_{\beta}(1+f_R)\omega\Delta\Phi - \\ \qquad \dfrac{1}{2}\Delta(\Phi u) + \Phi_L u_L f_L^*\Delta p_L^*, \qquad\qquad \text{if } m_{1/2} \geqslant 0, \\ -c_{1/2}\Phi_R\Delta Ma^{\beta+} - c_{1/2}Ma_L^+|_{\beta}(1+f_L)\omega\Delta\Phi + \\ \qquad \dfrac{1}{2}\Delta(\Phi u) + \Phi_R u_R f_R^*\Delta p_R^*, \qquad\qquad \text{else}, \end{cases} \tag{15}$$

$$F_D^P = -\frac{3+4\alpha}{4}\Delta(PMa) + \frac{1+8\alpha}{4}\Delta(PMa^3) - \frac{4\alpha}{4}\Delta(PMa^5). \tag{16}$$

3) If $|Ma_L| = \dfrac{|u_L|}{c_{1/2}} < 1$, $|Ma_R| = \dfrac{|u_R|}{c_{1/2}} \geqslant 1$,

$$F_D^{\Phi} = \begin{cases} c_{1/2}Ma_R^-|_{\beta}\omega\Delta\Phi - \dfrac{1}{2}[\Phi_L\Delta u_L^* + \Delta(\Phi_R u^*)] + \\ \qquad Ma_L^+|_{\beta}c_{1/2}\Phi_L f_L^*\Delta p_L^*, \qquad \text{if } m_{1/2} \geqslant 0, \\ -c_{1/2}Ma_L^+|_{\beta}(1+f_L)\omega\Delta\Phi - \dfrac{1}{2}[\Phi_R\Delta u_R^* + \Delta(\Phi_L u^*)] + \\ \qquad Ma_L^+|_{\beta}c_{1/2}\Phi_R f_L^*\Delta p_L^*, \qquad \text{else}, \end{cases} \tag{17}$$

$$F_D^P = P_L\Delta\mathcal{X}_L^* - \frac{1}{2}\Delta(\mathrm{sign}(Ma))P. \tag{18}$$

4) If $|Ma_L| = \dfrac{|u_L|}{c_{1/2}} \geqslant 1$, $|Ma_R| = \dfrac{|u_R|}{c_{1/2}} < 1$,

$$F_D^{\Phi} = \begin{cases} c_{1/2}Ma_R^-|_{\beta}(1+f_R)\omega\Delta\Phi - \dfrac{1}{2}[\Phi_L\Delta(u_L^*) + \Delta(\Phi_R u^*)] + \\ \qquad Ma_R^-|_{\beta}c_{1/2}\Phi_L f_R^*\Delta p_R^*, \qquad \text{if } m_{1/2} \geqslant 0, \\ -c_{1/2}Ma_L^+|_{\beta}\omega\Delta\Phi - \dfrac{1}{2}[\Phi_R\Delta(u_R^*) + \Delta(\Phi_L u^*)] + \\ \qquad Ma_R^-|_{\beta}c_{1/2}\Phi_R f_R^*\Delta p_R^*, \qquad \text{else}, \end{cases} \tag{19}$$

$$F_D^P = -P_R\Delta\mathcal{X}_R^* - \frac{1}{2}\Delta(\mathrm{sign}(Ma)P). \tag{20}$$

In eqs.(13) to (20),

$$\Delta\Phi = \Phi_R - \Phi_L, \ \Delta|u| = |u_R| - |u_L|,$$
$$\Delta\mathrm{sign}(u) = \mathrm{sign}(u_R) - \mathrm{sign}(u_L), \ \Delta P = P_R - P_L,$$
$$\Delta Ma^{\beta\pm} = Ma_R^{\beta\pm} - Ma_L^{\beta\pm}, \ \Delta(\Phi u) = \Phi_R u_R - \Phi_L u_L,$$
$$\Delta p_{L,R}^* = p_{L,R} - p_s, \ \Delta u_{L,R}^* = u_{L,R} - u_{1/2},$$
$$\Delta(PMa) = P_R Ma_R - P_L Ma_L, \ \Delta(PMa^3) = P_R Ma_R^3 - P_L Ma_L^3,$$

$$\Delta(\boldsymbol{P}Ma^5) = \boldsymbol{P}_{\mathrm{R}}Ma_{\mathrm{R}}^5 - \boldsymbol{P}_{\mathrm{L}}Ma_{\mathrm{L}}^5,$$

$$\Delta(\boldsymbol{\Phi}_{\mathrm{R}}u^*) = \boldsymbol{\Phi}_{\mathrm{R}}u_{\mathrm{R}} - \boldsymbol{\Phi}_{\mathrm{L}}u_{1/2}, \ \Delta(\boldsymbol{\Phi}_{\mathrm{L}}u^*) = \boldsymbol{\Phi}_{\mathrm{L}}u_{\mathrm{L}} - \boldsymbol{\Phi}_{\mathrm{R}}u_{1/2},$$

$$\Delta(\mathrm{sign}(Ma)\boldsymbol{P}) = \mathrm{sign}(Ma_{\mathrm{R}})\boldsymbol{P}_{\mathrm{R}} - \mathrm{sign}(Ma_{\mathrm{L}})\boldsymbol{P}_{\mathrm{L}},$$

$$\Delta X_{\mathrm{L,R}}^* = X(Ma_{\mathrm{L,R}}) - X(\mathrm{sign}(Ma_{\mathrm{L,R}})),$$

where

$$Ma_{\mathrm{L,R}} = \frac{u_{\mathrm{L,R}}}{c_{1/2}}, \ Ma_{\mathrm{L,R}}^{\beta\pm} = \left[\frac{1}{4}(Ma_{\mathrm{L,R}} \pm 1)^2 + \beta(Ma_{\mathrm{L,R}}^2 - 1)^2\right](1 + f_{\mathrm{L,R}}),$$

$$Ma_{\mathrm{L,R}}^{\pm}|_{\beta} = \begin{cases} \pm\dfrac{1}{4}(Ma_{\mathrm{L,R}} \pm 1)^2 \pm \beta(Ma_{\mathrm{L,R}}^2 - 1)^2, & \text{if } |Ma_{\mathrm{L,R}}| < 1, \\ \dfrac{1}{2}(Ma_{\mathrm{L,R}} \pm |Ma_{\mathrm{L,R}}|), & \text{else}, \end{cases}$$

$$X(Ma) = \left(\frac{3}{4} + \alpha\right)Ma - \left(\frac{1}{4} + 2\alpha\right)Ma^3 + \alpha Ma^5,$$

$$u_{1/2} = m_{1/2}c_{1/2}, \ m_{1/2} = Ma_{\mathrm{L}}^+|_{\beta=1/8} + Ma_{\mathrm{R}}^-|_{\beta=1/8},$$

$$c_{1/2} = \min(\tilde{c}_{\mathrm{L}}, \tilde{c}_{\mathrm{R}}), \ \tilde{c}_{\mathrm{L,R}} = \frac{c_{\mathrm{L,R}}^{*2}}{\max(|u_{\mathrm{L,R}}|, c_{\mathrm{L,R}}^*)}, \ c_{\mathrm{L,R}}^* = \sqrt{\frac{2(\gamma-1)}{\gamma+1}H_{\mathrm{L,R}}},$$

$$H = \frac{\gamma}{\gamma-1}\frac{p}{\rho} + \frac{u^2}{2}, \ p_s = P_{\mathrm{L}}^+|_{\alpha=3/16}p_{\mathrm{L}} + P_{\mathrm{R}}^-|_{\alpha=3/16}p_{\mathrm{R}},$$

$$C_{\mathrm{pl}}(x,y) = \begin{cases} 4 \times \min\left(\dfrac{x}{y}, \dfrac{y}{x}\right) - 3, & \text{if } \dfrac{3}{4} \leqslant \min\left(\dfrac{x}{y}, \dfrac{y}{x}\right) < 1, \\ 0, & \text{else}, \end{cases}$$

$$f_{\mathrm{L,R}} = \begin{cases} \left(\dfrac{p_{\mathrm{L,R}}}{p_s} - 1\right)C_{\mathrm{pl}}(p_{\mathrm{L,R}}, p_{\mathrm{R,L}}) \times |Ma_{\mathrm{L,R}}^{\pm}|_{\beta=0} \times \min\left(1, \dfrac{|u_{\mathrm{L,R}}|}{c_{1/2}}\right)^{0.25}, \\ \qquad\qquad\qquad\qquad\qquad\qquad\qquad \text{if } |Ma_{\mathrm{L,R}}| \leqslant 1, \\ 0, \qquad\qquad\qquad\qquad\qquad\qquad\qquad \text{else}, \end{cases}$$

$$P^{\pm}|_{\alpha} = \begin{cases} \dfrac{1}{4}(Ma \pm 1)^2(2 \mp Ma) \pm \alpha Ma(Ma^2 - 1)^2, & \text{if } |Ma| < 1, \\ \dfrac{1}{2}(1 \pm \mathrm{sign}(Ma)), & \text{else}, \end{cases}$$

$$\omega = \omega(p_{\mathrm{L}}, p_{\mathrm{R}}) = 1 - \min\left(\frac{p_{\mathrm{L}}}{p_{\mathrm{R}}}, \frac{p_{\mathrm{R}}}{p_{\mathrm{L}}}\right)^3.$$

2   Numerical tests

Eqs.(8),(9) and (12) indicate that flux dissipations are nearly proportional to flow jumps with coefficient $C(U^{\mathrm{m}})$ as a function of some intermediate flow values between U^{L} and U^{R}. In most cases, low jumps, namely small values of ΔU, result in low flux dissipations. It may be expected that the cell-edge flow jumps acquired through high-order reconstructions (or interpolations) are usually lower than those through low-order reconstructions (or interpolations). Then, for high-order schemes, flux dissipations are usually low

and their unfavorable influences on the accuracy of numerical results shall also be low. These statements will be illustrated by the following tests.
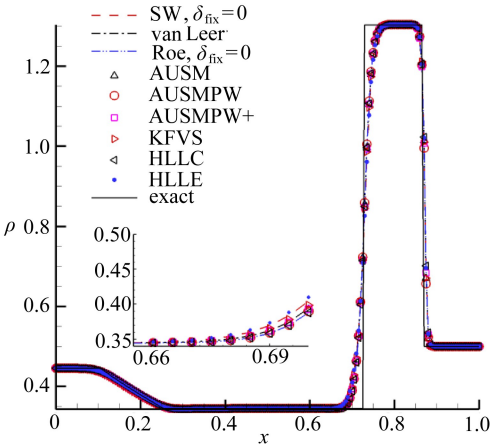
2.1 Lax's shock tube

The 1st test is chosen to investigate the properties of different fluxes in resolving the contact discontinuity as well as the shock wave. 1D Euler equations are solved numerically. The spatial domain is $x \in [0,1]$, and the initial conditions are defined as
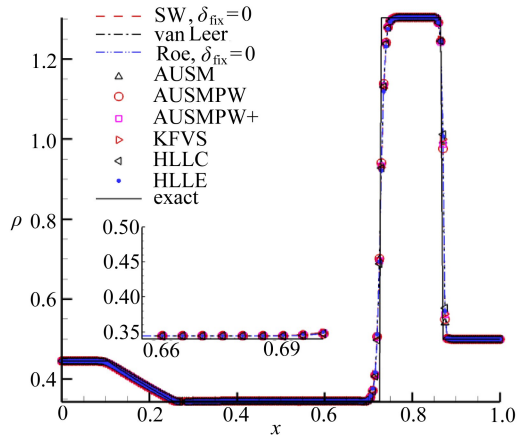
$$\begin{cases} [\rho, u, p] = [0.445, 0.698, 0.352\ 8], & \text{if } x < 0.5, \\ [\rho, u, p] = [0.500, 0.000, 0.517\ 0], & \text{if } x \geqslant 0.5. \end{cases} \quad (21)$$
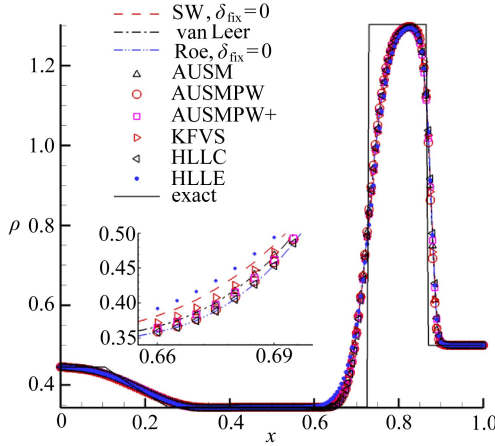
(a) The 1st-order scheme

(b) The NND scheme (2nd-order)

(c) The WCNS scheme (5th-order)

Fig. 1   Results of Lax's shock tube

We computed the solution up to time $t = 0.15$ with 200 cells. Numerical results are given in fig. 1. Obvious improvement is reached with the increase of the accuracy order of spatial schemes. In contrast to the 1st-order upwind scheme and the 2nd-order NND scheme, the high-order WCNS gives almost indistinguishable differences between different fluxes, which indicates that the influence of inviscid flux functions on this flow will be diminished with the increase of the accuracy orders of spatial discretization schemes. In order to study

the resolving powers of different fluxes for the contact discontinuity more clearly, we de-
fine the averaged errors of density in the domain of $x_i \in [0.6, 0.825]$ which contains the
contact discontinuity,

$$\varepsilon_\rho = \frac{1}{46} \sum_i |\rho_i^{\text{num}} - \rho_i^{\text{exact}}|. \tag{22}$$

The averaged errors of density are given in fig. 2. It can be seen that, when the 1st-order
upwind scheme is applied to the inviscid fluxes, the HLLE flux shows the highest dissipa-
tion for this contact discontinuity, while Roe's flux, the HLLC and the AUSMPW show the
lowest dissipations. Fig. 2 also indicates that the differences between the fluxes are only
visible for the 1st-order scheme. When the high-order scheme is used, the difference be-
tween the highest dissipative flux (HLLE) and the lowest dissipative fluxes (Roe's, the
HLLC and the AUSMPW) is trivial.
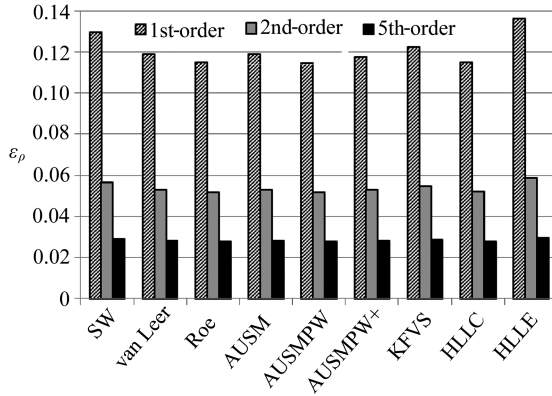
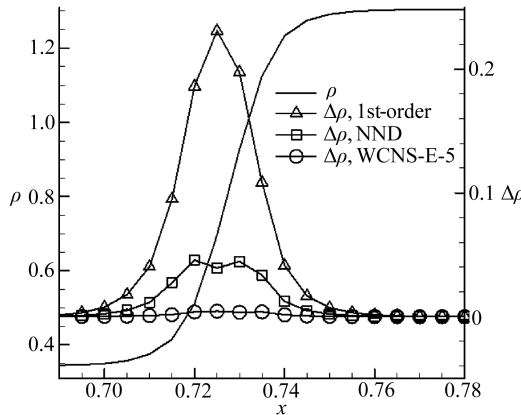Fig. 2   Numerical errors around the contact discontinuity

Fig. 3   Density distributions and their jumps at cell edges ($\Delta\rho = |\rho^{\text{R}} - \rho^{\text{L}}|$)

The differences between fluxes are neglectable for the high-order method because the
cell-edge jumps ($\Delta U_{i+1/2} = U_{i+1/2}^{\text{R}} - U_{i+1/2}^{\text{L}}$) are much low. The flow jumps occur due to the
different reconstructions (or interpolations) at the left/right side of the interface. Fig. 3
shows the density jumps near the contact discontinuity. It is evident that the 1st-order
scheme produces the highest jump, the 2nd-order scheme (NND) produces the intermedi-

ate jump, and the 5th-order scheme (WCNS-E-5) produces the lowest jump. The lowest jump is less than 2% of the highest jump. As flux dissipations are nearly proportional to the jumps, from the view point of dissipation, the high-order schemes are less sensitive to flux construction methods than the low-order schemes.

2.2 Viscous hypersonic flow around a hemicylinder

This example is used to investigate the influences of different inviscid fluxes on the computations of stagnation heat transfer rates in the conditions of different grid densities and spatial accuracy orders. The freestream Mach number is 5.73, static temperature 39.67 K, surface temperature 210.2 K, $\gamma = 1.4$ and $Pr = 0.77$. The Reynolds number based on the cylinder radius is 2 050. A numerical solution is available in ref. [39] where a shock-fitted Chebyshev spectral method is used.
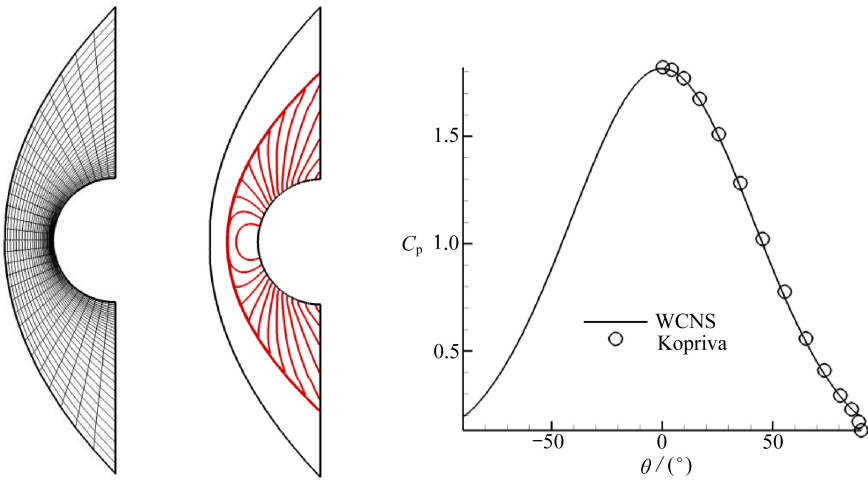

Fig. 4　The grid (left), the pressure contour(middle) and the surface pressure (right)

6 grids are generated for this problem. A typical grid and the solution are given in fig. 4. The minimal grid size h_m of the coarsest grid is 20/2 050 of the cylinder radius. Thus the grid Reynolds number Re_h (based on the minimal grid size) is 20. The Re_h of the 6 grids can be found in tables 2 ~ 4 which also contain the normalized stagnation heat transfer rates (normalized by $\rho_\infty u_\infty^3$). Symbol "unst" in the 3 tables denotes that the carbuncle phenomenon appears or the solution is unstable. Table 4 indicates that the computed results of the high-order method converge at 1.248×10^{-2}. Fig. 5 shows the stagnation heatings vs. the grid Reynolds number (Re_h). Fig. 5(a) and (b) indicate that the results of the 1st-order method and the 2nd-order method show the trend of converging at 1.248×10^{-2} with the refinement of the grids.

This case shows the signal that the high-order method may be superior to the 2 low-order methods in converging to grid-independence results. In addition, the followings can be observed:

1) The 1st-order method is more sensitive to grid sizes than the 2nd-order and the 5th-order methods. When the 1st-order scheme is used, the FVSs (such as SW, KFVS, van Leer) generally require smaller grid sizes for heating computation than low dissipative

FDSs (such as AUSMPW and Roe's flux). When the spatial accuracy order increases, the influences of inviscid fluxes on the stagnation heat transfer rate will decrease.
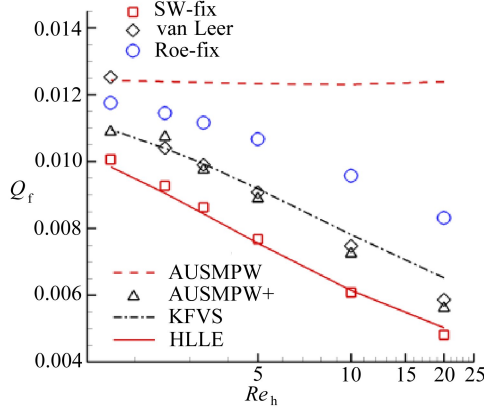
Table 2   Stagnation heat transfer rates computed with the 1st-order upwind scheme

grid point	31×31	61×61	121×121	181×181	241×241	361×361
Re_h	20	10	5	3.33	2.50	1.67
SW	unst	unst	unst	unst	unst	unst
SW-fix	4.812E−3	6.088E−3	7.683E−3	8.637E−3	9.273E−3	1.007E−2
VL	5.870E−3	7.472E−3	9.083E−3	9.905E−3	1.041E−2	1.252E−2
Roe	unst	unst	unst	unst	unst	unst
Roe-fix	8.314E−3	9.578E−3	1.067E−2	1.116E−2	1.144E−2	1.175E−2
AUSMPW	1.238E−2	1.231E−2	1.233E−2	1.236E−2	1.239E−2	1.243E−2
AUSMPW+	5.616E−3	7.236E−3	8.891E−3	9.748E−3	1.073E−2	1.088E−2
KFVS	6.523E−3	7.809E−3	9.185E−3	9.928E−3	1.040E−2	1.095E−2
HLLC-p	1.437E−2	unst	unst	unst	unst	unst
HLLC-Roe	1.441E−2	unst	unst	unst	unst	unst
HLLE	5.024E−3	6.148E−3	7.557E−03	8.440E−3	9.049E−3	9.841E−3

Table 3   Stagnation heat transfer rates computed with the 2nd-order NND scheme

| grid point	31×31	61×61	121×121	181×181	241×241	361×361
Re_h	20	10	5	3.33	2.50	1.67
SW	1.308E−2	1.293E−2	1.268E−2	1.255E−2	1.255E−2	1.254E−2
SW-fix	1.354E−2	1.319E−2	1.279E−2	1.263E−2	1.260E−2	1.256E−2
VL	1.349E−2	1.293E−2	1.260E−2	1.256E−2	1.255E−2	1.282E−2
Roe	1.312E−2	unst	unst	unst	unst	unst
Roe-fix	1.378E−2	1.294E−2	1.258E−2	1.255E−2	1.254E−2	1.251E−2
AUSMPW	1.274E−2	1.225E−2	1.251E−2	1.243E−2	1.247E−2	1.247E−2
AUSMPW+	1.348E−2	1.285E−2	1.250E−2	1.254E−2	1.254E−2	1.251E−2
KFVS	1.410E−2	1.329E−2	1.273E−2	1.264E−2	1.260E−2	1.255E−2
HLLC-p	1.312E−2	unst	unst	unst	1.248E−2	unst
HLLC-Roe	1.312E−2	unst	unst	unst	1.248E−2	unst
HLLE	1.441E−2	1.364E−2	1.290E−2	1.275E−2	1.269E−2	1.260E−2

Table 4   Stagnation heat transfer rates computed with the 5th-order WCNS scheme

| grid point	31×31	61×61	121×121	181×181	241×241	361×361
Re_h	20	10	5	3.33	2.50	1.67
SW	1.263E−2	1.256E−2	1.249E−2	1.243E−2	1.247E−2	1.248E−2
SW-fix	1.264E−2	1.257E−2	1.249E−2	1.244E−2	1.247E−2	1.248E−2
VL	1.274E−2	1.254E−2	1.238E−2	1.246E−2	1.247E−2	1.248E−2
Roe	1.336E−2	1.271E−2	1.237E−2	1.248E−2	1.248E−2	1.248E−2
Roe-fix	1.313E−2	1.269E−2	1.241E−2	1.246E−2	1.248E−2	1.248E−2
AUSMPW	1.312E−2	1.260E−2	1.249E−2	1.247E−2	1.247E−2	1.248E−2
AUSMPW+	1.274E−2	1.253E−2	1.240E−2	1.247E−2	1.247E−2	1.248E−2
KFVS	1.282E−2	1.263E−2	1.239E−2	1.245E−2	1.247E−2	1.248E−2
HLLC-p	1.336E−2	1.271E−2	1.242E−2	1.248E−2	1.248E−2	1.248E−2
HLLC-Roe	1.336E−2	1.271E−2	1.250E−2	1.248E−2	1.248E−2	1.248E−2
HLLE	1.261E−2	1.259E−2	1.245E−2	1.248E−2	1.248E−2	1.248E−2

2) The effects of inviscid fluxes on the accuracy (not on the numerical stability) of computed resutls can be effectively eliminated through either high-order discretizations or grid refinement, which suggests that other factors such as viscous discretizations and limiters shall be considered in advance of more accurate simulations.

(a) The 1st-order upwind
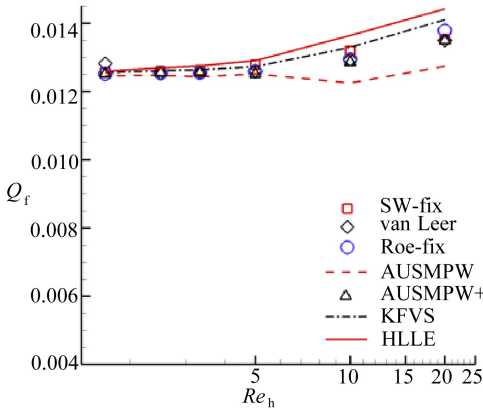
(b) The NND (2nd-order)
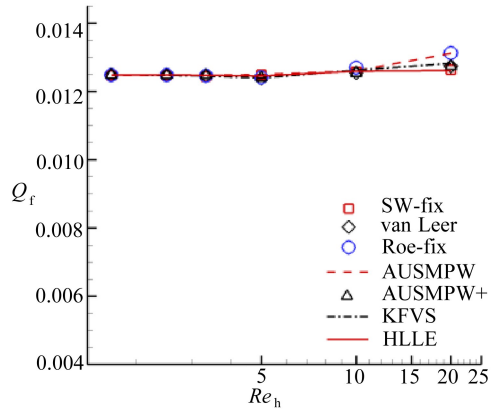
(c) The WCNS (5th-order)

Fig. 5   The grid convergences of the stagnation heat transfer rates

2.3   SWBLI of an axisymmetric hollow-cylinder flare

It is well known that hypersonic flows exhibit many difficulties in CFD because of lots of special phenomena and flow characteristics, such as compressibility effects, real gas effects, strong shock waves and SWBLI which may induce separations and heat flux enhancements[20,22,40]. This test is chosen to examine the flux properties in simulating SWBLI. The configuration is shown in fig. 6(a). This is an axisymmetric hollow cylinder with its symmetry axis along the flow direciton. A 30-deg. flare adheres to the cylinder at the downstream end. The static temperature of the incoming mean flow is 120.4 K, and the Mach number is 10.3. The Reynolds number is 25 347 (based on L = 4.004 in(1 in = 2.54 cm)). The no-slip wall condition is applied to the surface with an isothermal temperature of 295.2 K. The flow medium is pure nitrogen, which can minimize chemical nonequilibrium effects. Please refer to ref. [41] for more details about the windtunnel experiments. The studies of

Kirk and Carey[42] and the references therein show that the gas can be regareded as calorically perfect.

（a）The model configuration（unit: in）

（b）The 231×81 grid

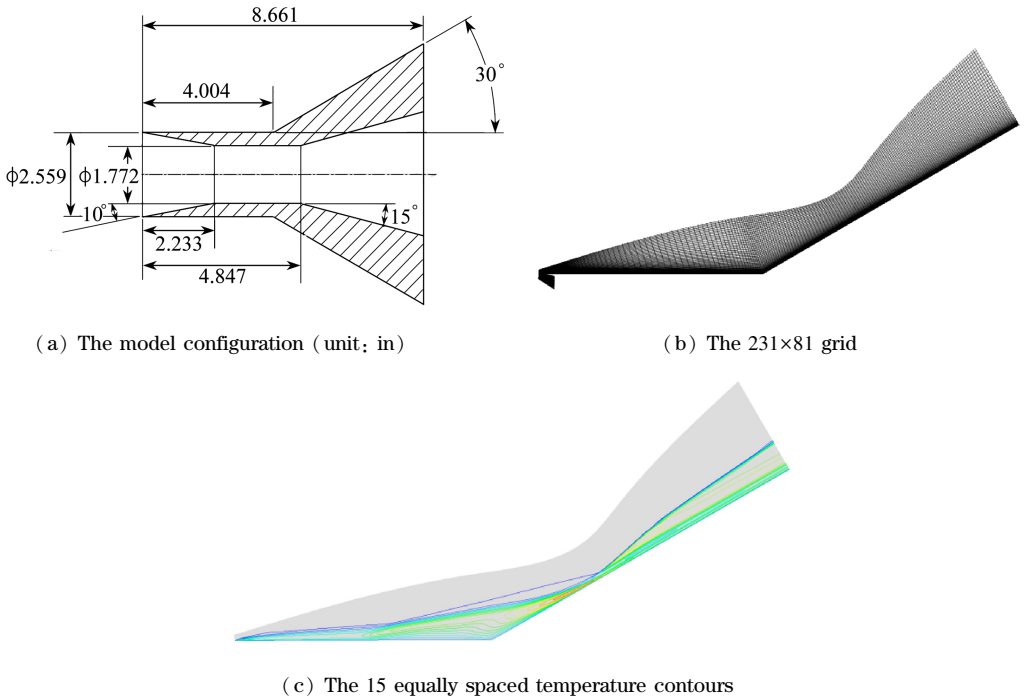（c）The 15 equally spaced temperature contours

Fig. 6　The model configuration, the grids and temperature contours for the hollow-cylinder flare

3 computational grids are used in this test. The coarse grid contains 231×81 （streamwise × wall-normal） nodes, and the medium and fine grids contain 461×161 nodes and 691 ×241 nodes, respectively. The coarse grid is shown in fig. 6(b), and the computed temperatures on the coarse grid are shown in fig. 6(c). Fig. 7 shows the heat transfer rates and pressure coefficients computed with the WCNS-E-5 scheme for the coarse mesh. One can find that the influences of different inviscid fluxes on the computed results are not very obvious. A close examination of the numerical solutions shows that the largest differences bewteen the computed results from variant flux functions occur at the maximum values. The maximum difference between the heat transfer rates is nearly 11.4%, and the maximum difference between the pressure coefficients is nearly 3%. The entropy fix shows trivial influence on the results except the maximum heat transfer rate and the maximum pressure coefficient, e.g. the entropy fix causes the maximum heat transfer rates to decrease by 9. 6% and 8.7% for Roe's flux and the SW flux, respectively. Grid refinement can effectively reduce the influence of flux functions. Fig. 8 shows the numerical results from the medium grid. It is obvious that all the fluxes produce almost identical results. The maximum differences in heat transfer rates and pressure coefficients are only 2.9% and 2.5%, respectively. However, as shown in fig. 9, compared with the WCNS-E-5 scheme, the 2nd-order method are much more sensitive to grid density.

Because of the strong SWBLI, there is a separation bubble at the compression corner.

The detachment point and the reattachment point of the separation bubble can be clearly identified in fig. 10. At the reattachment point there are local high temperature gradients, high pressure loads and high surface heat transfer rates (fig. 7 to fig. 9). The surface pressure and heat transfer rate get their maxima at an x/L value of approximately 1.45, which is slightly downstream from the reattachment point. Fig. 7 and fig. 10(a) show that, when the high-order method is used, only KFVS gives a slightly smaller separation bubble on the coarse grid, which indicates that KFVS contains the highest dissipation among the tested fluxes for the present flow. However, the 2nd-order method tends to give a smaller separation bubble. As shown in fig. 9 and fig. 10(b), compared with the high-order method, the 2nd-order method is more sensitive to grid density and tends to give a smaller separation bubble, e.g. its separation bubble on the coarse grid is approximately 34% smaller than that of the high-order scheme on the same grid. Once the grid is refined, the separation bubble will increase. This phenomenon is consistent with the observation that the size of a laminar separated bubble will grow when the Reynolds number increaes[42]. This phenomenon indicates a low-density grid adds additional numerical diffusion with the low-order scheme.
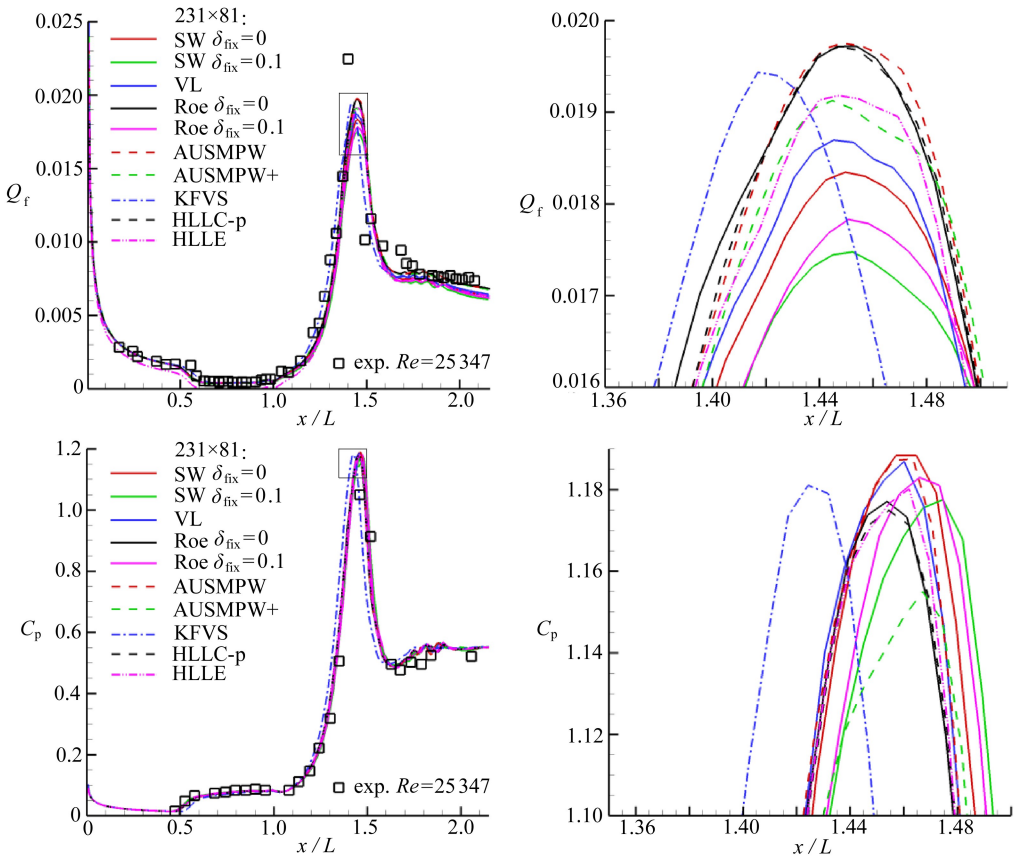

Fig. 7　Flux comparison of heat transfer rates and pressure coefficients acquired with the WCNS-E-5 method on the 231×81 grid(the right-hand diagrams are the enlarged parts around the peak values of the left-hand diagrams)
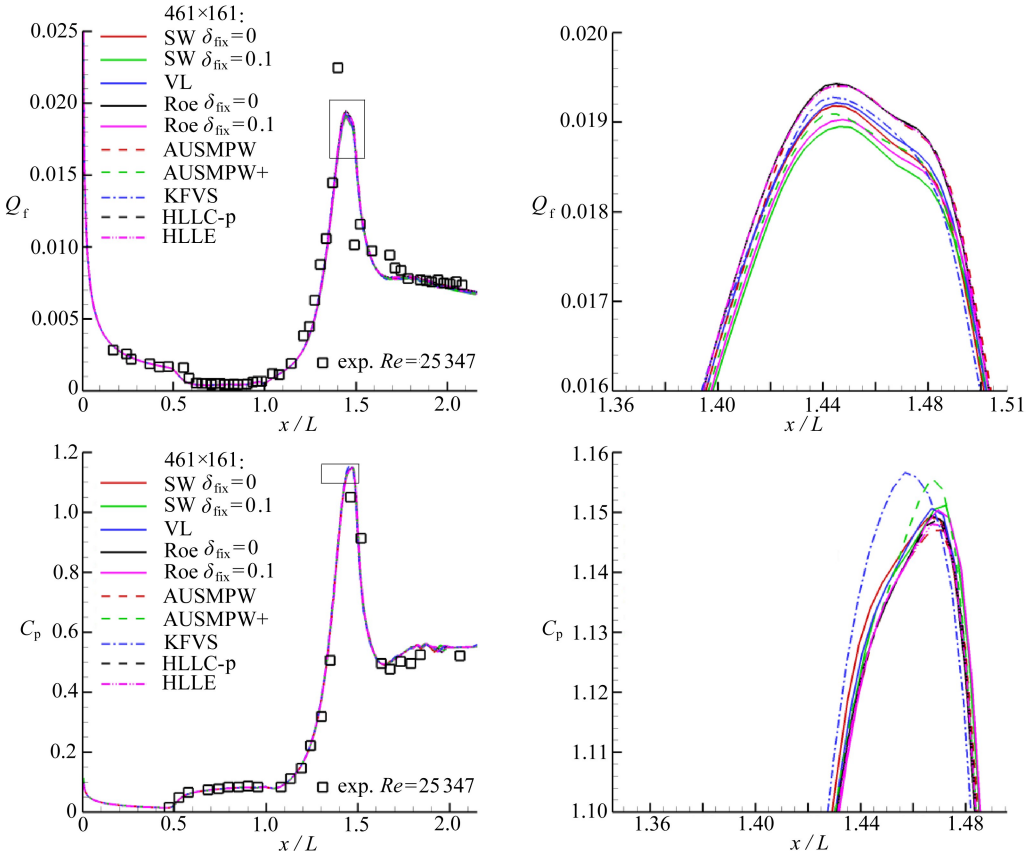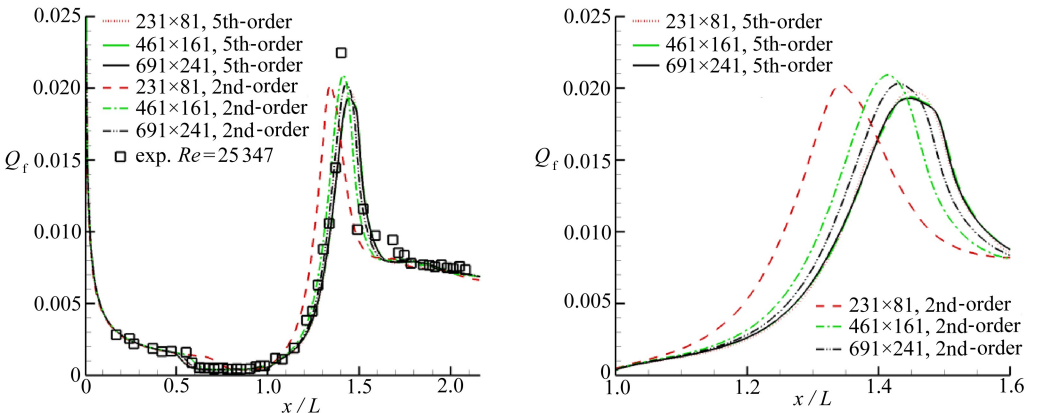
Fig. 8   Flux comparison of heat transfer rates and pressure coefficients acquired with the
WCNS-E-5 method on the 461×161 grid(the right-hand diagrams are the enlarged
parts around the peak values of the left-hand diagrams)

Fig. 7 and fig. 8 indicate that fluxes' influences on the accuracy of numerical results are small for the high-order scheme, and can be effectively diminished through grid refinement. However, for low-order schemes, it was reported in literatures that the flux functions had strong influences on both shock instability and surface heating computations[19-23]. Our computation tests tell that both the flux functions and the grid density have direct influences on the results from low-order schemes.
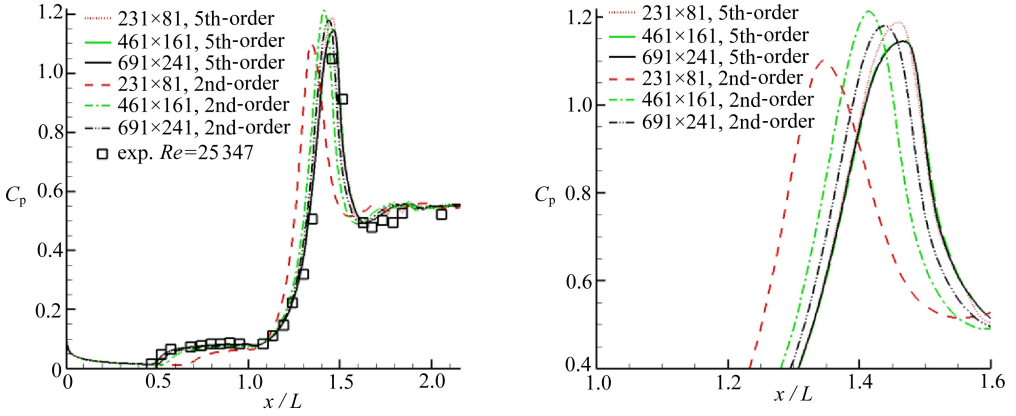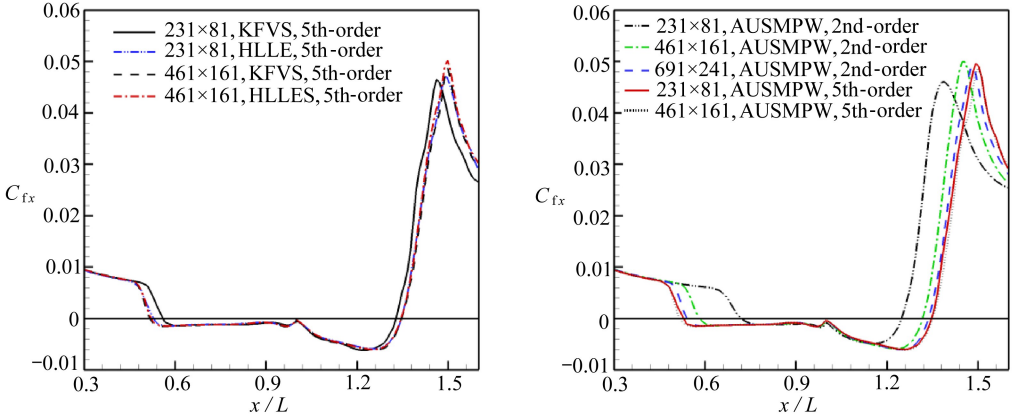
Fig. 9   Comparison between the high-order scheme and the low-order scheme for the
hollow-cylinder flare based AUSMPW flux(the right-hand diagrams are the
enlarged parts around the peak values of the left diagrams)

It can be found from fig. 7 to fig. 9 that the peak heat transfer rates measured in the wind tunnel exceed the computed values, and similar results were reported in ref. [42] and the references therein. The reasons for this discrepancy are still unknown.

(a) Acquired with the high-order methods

(b) Comparison between the high-order and
2nd-order schemes

Fig. 10   The axial component of the skin friction coefficient

3   Concluding remarks

Inviscid fluxes are divided into central terms and dissipation terms. The central terms are acquired by averaging the left-hand values and the right-hand values at cell interfaces (cell edges), while the dissipation terms are more or less complicated and different flux functions have different dissipations. The analysis on inviscid fluxes shows that flux dissipations can be computed by multiplying cell-edge flow jumps by some intermediate flow values between left-hand and right-hand values. Then, flux dissipations are nearly proportional to cell-edge flow jumps in smooth regions.

The influences of inviscid fluxes on surface heating computations are investigated with

a 5th-order weighted compact nonlinear scheme（WCNS-E-5）and 2 low-order schemes （2nd order and 1st order）. The numerical results indicate that, compared with low-order methods, the high-order method produces much lower cell-edge flow jumps, and then much lower dissipations. Thus, the unfavorable influences of flux constructions on surface heating are minor for high-order schemes, and can be effectively diminished through grid refinement. Note the constructions of inviscid fluxes do have significant influences on shock instability or shock anomalies（such as carbuncle phenomena）as shown in some references. In addition to diminishing the adverse influences of flux dissipations on surface heating computations, the high-order numerical methods（if they do not blow up）may be superior to the low-order ones in the aspect of producing reasonable grid-independent numerical results on relatively coarse grids.

When the high-order method is used, based on the present study and the related studies in the previous literatures, we recommend selecting inviscid fluxes with high shock stabilities, and selecting low-dissipation fluxes only on the premise of high shock stabilities.

Acknowledgments

References：

［1］   Ekaterinaris J A. High-order accurate, low numerical diffusion methods for aerodynamics［J］. *Progress in Aerospace Sciences*, 2005, **41**（3/4）: 192-300.

［2］   DENG Xiao-gang, MAO Mei-liang, TU Guo-hua, ZHANG Han-xin, ZHANG Yi-feng. High-order and high accurate CFD methods and their applications for complex grid problems［J］. *Communications in Computational Physics*, 2012, **11**（4）: 1081-1102.

［3］   DENG Xiao-gang, MAO Mei-liang, TU Guo-hua, LIU Hua-yong, ZHANG Han-xin. Geometric conservation law and applications to high-order finite difference schemes with stationary grids ［J］. *Journal of Computational Physics*, 2011, **230**（4）: 1100-1115.

［4］   DENG Xiao-gang, MAO Mei-liang, TU Guo-hua, ZHANG Yi-feng, ZHANG Han-xin. Extending weighted compact nonlinear schemes to complex grids with characteristic-based interface conditions［J］. *AIAA Journal*, 2010, **48**（12）: 2840-2851.

［5］   TU Guo-hua, DENG Xiao-gang, MAO Mei-liang. Implementing high-order weighted compact nonlinear scheme on patched grids with a nonlinear interpolation［J］. *Computers & Fluids*, 2013, **77**: 181-193.

［6］   TU G, Deng X, Liu H, Zhao X. Validation of high-order weighted compact nonlinear scheme for heat transfer of complex hypersonic laminar flows［C］//*The 4th Asian Symposium on Computational Heat Transfer and Fluid Flow*. Hong Kong, 2013: ASCHT0095-T01-2-A.

［7］   Rizzetta D P, Viabal M R, Morgan P E. A high-order compact finite-difference scheme for large-eddy simulation of active flow control［J］. *Progress in Aerospace Sciences*, 2008, **44** （6）: 397-426.

［8］   Pirozzoli S. Numerical methods for high-speed flows［J］. *Annual Review of Fluid Mechanics*,

2011, **43**：163-194.

[9]   DENG Xiao-gang, ZHANG Han-xin. Developing high-order weighted compact nonlinear schemes
       [J]. *Journal of Computational Physics*, 2000, **165**(1)：22-44.

[10]   Cockburn B, Shu C. The Runge-Kutta discontinuous Galerkin method for conservation laws
       V：multidimensional systems[J]. *Journal of Computational Physics*, 1998, **141**(2)：199-224.

[11]   TU Guo-hua, YUAN Xiang-jiang, XIA Zhi-qiang, HU Zhen. A class of compact upwind TVD
       difference schemes[J]. *Applied Mathematics and Mechanics*, 2006, **27**(6)：675-682.

[12]   TU Guo-hua, YUAN Xiang-jiang, LU Li-peng. Developing shock-capturing difference methods
       [J]. *Applied Mathematics and Mechanics*, 2007, **28**(4)：433-440.

[13]   TU Guo-hua, YUAN Xiang-jiang. A characteristic-based shock-capturing scheme for hyperbol-
       ic problems[J]. *Journal of Computational Physics*, 2007, **225**(2)：2083-2097.

[14]   Shu C. High order weighted essentially nonoscillatory schemes for convection dominated
       problems[J]. *SIAM Review*, 2009, **51**(1)：82-126.

[15]   Wang Z J. High-order methods for the Euler and Navier-Stokes equations on unstructured
       grids[J]. *Progress in Aerospace Sciences*, 2007, **43**(1/3)：1-41.

[16]   Suresh A, Huynh H T. Accurate monotonicity-preserving schemes with Runge-Kutta time step-
       ping[J]. *Journal of Computational Physics*, 1997, **136**(1)：83-99.

[17]   TU Guo-hua, DENG Xiao-gang, MAO Mei-liang. Assessment of two turbulence models and
       some compressibility corrections for hypersonic compression corners by high-order difference
       schemes[J]. *Chinese Journal of Aeronautics*, 2012, **25**(1)：25-32.

[18]   XU Chuan-fu, DENG Xiao-gang, ZHANG Li-lun, FANG Jian-bin, WANG Guang-xue, JIANG
       Yi, GAO Wei, CHE Yong-gang, WANG Zheng-hua, LIU Wei, CHENG Xing-hua. Collaborating
       CPU and GPU for large-scale high-order CFD simulations with complex grids on the TianHe-
       1A supercomputer[J]. *Journal of Computational Physics*, 2014, **278**(1)：275-297.

[19]   Kitamura K. Afurther survey of shock capturing methods on hypersonic heating issues[C]//
       21st AIAA Computational Fluid Dynamics Conference. San Diego, CA, 2013：2013-2698.

[20]   Kitamura K, Shima E, Roe P L. Carbuncle phenomena and other shock anomalies in three di-
       mensions[J]. *AIAA Journal*, 2012, **50**(12)：2655-2669.

[21]   Kitamura K, Roe P, Ismail F. Evaluation of Euler fluxes for hypersonic flow computations
       [J]. *AIAA Journal*, 2009, **47**(1)：44-53.

[22]   Kitamura K, Shima E, Nakamura Y, Roe P. Evaluation of Euler fluxes for hypersonic heating
       computations[J]. *AIAA Journal*, 2010, **48**(4)：763-776.

[23]   TU Guo-hua, ZHAO Xiao-hui, MAO Mei-liang, CHEN Jian-qiang, DENG Xiao-gang, LIU Hua-
       yong. Evaluation of Euler fluxes by a high-order CFD scheme：shock instability[J]. *Interna-
       tional Journal of Computational Fluid Dynamics*, 2014, **28**(5)：171-186.

[24]   Pandolfi M, D'Ambrosio D. Numerical instabilities in upwind methods：analysis and cures for
       the "carbuncle" phenomenon[J]. *Journal of Computational Physics*, 2001, **166**(2)：271-
       301.

[25]   van Leer B. Flux-vector splitting for the Euler equation[M]//*Upwind and High-Resolution
       Schemes*. Berlin：Springer Berlin Heidelberg, 1997：80-89.

[26]   Steger J L, Warming R F. Flux vector splitting of the inviscid gasdynamic equations with ap-
       plication to finite-difference methods[J]. *Journal of Computational Physics*, 1981, **40**(2)：
       263-293.

[27]   Mandal J C, Deshpande S M. Kinetic flux vector splitting for Euler equations[J]. *Computers &*

Fluids, 1994, **23**(2): 447-478.

[28]　Roe P L. Approximate Riemann solvers, parameter vectors, and difference schemes[J]. *Journal of Computational Physics*, 1981, **43**(2): 357-372.

[29]　Liou M S. Mass flux schemes and connection to shock instability[J]. *Journal of Computational Physics*, 2000, **160**(2): 623-648.

[30]　Kim K H, Lee J H, Rho O H. An improvement of AUSM schemes by introducing the pressure-based weight functions[J]. *Computers & Fluids*, 1998, **27**(3): 311-346.

[31]　Kim K H, Kim C, Rho O H. Methods for the accurate computations of hypersonic flows—I: AUSMPW+ scheme[J]. *Journal of Computational Physics*, 2001, **174**(1): 38-80.

[32]　Einfeldt B, Munz C D, Roe P L, Sjögreen B. On Godunov-type methods near low densities [J]. *Journal of Computational Physics*, 1991, **92**(2): 273-295.

[33]　Harten A, Lax P D, van Leer B. On upstream differencing and Godunov-type schemes for hyperbolic conservation laws[M]//*Upwind and High-Resolution Schemes*. Berlin: Springer Berlin Heidelberg, 1997: 53-79.

[34]　Batten P, Clarke N, Lambert C, Causon D M. On the choice of wavespeeds for the HLLC Riemann solver[J]. *SIAM Journal on Scientific Computing*, 1997, **18**(6): 1553-1570.

[35]　Toro E F. *Riemann Solvers and Numerical Methods for Fluid Dynamics: A Practical Introduction*[M]. 3rd ed. Springer, 2009.

[36]　ZHANG Han-xin, ZHUANG Feng-gan. NND schemes and their applications to numerical simulation of two- and three-dimensional flows[J]. *Advances in Applied Mechanics*, 1991, **29**: 193-256.

[37]　TU Guo-hua, DENG Xiao-gang, MAO Mei-liang. A staggered non-oscillatory finite difference method for high-order discretization of viscous terms[J]. *Acta Aerodynamica Sinica*, 2011, **29**(1): 10-15.

[38]　DENG Xiao-gang, MAO Mei-liang, TU Guo-hua, LIU Hua-yong, ZHANG Han-xin. Geometric conservation law and applications to high-order finite difference schemes with stationary grids [J]. *Journal of Computational Physics*, 2011, **230**(4): 1100-1115.

[39]　Kopriva D A. Spectral solution of the viscous blunt-body problem[J]. *AIAA Journal*, 1993, **31** (7): 1235-1242.

[40]　Longo J M A, Hannemann K, Hannemann V. The challenge of modeling high speed flows [C]//*The EUROSIM*. 2007.

[41]　Holden M S, Wadhams T P. A database of aerothermal measurements in hypersonic flow "building block" experiment for CFD validation[C]//*41st AIAA Aerospace Sciences Meeting and Exhibit*. Reno, Nevada, 2003: AIAA 2003-1137.

[42]　Kirk B S, Carey G F. Validation of fully implicit, parallel finite element simulations of laminar hypersonic flows[J]. *AIAA Journal*, 2010, **48**(6): 1025-1036.

关于高阶精度 WCNS 格式的无粘通量分裂方法

涂国华[1]，陈坚强[1,2]，毛枚良[1,2]，赵晓慧[1]，刘化勇[1]

(1. 空气动力学国家重点实验室(中国空气动力研究与发展中心)，四川 绵阳 621000；
2. 中国空气动力研究与发展中心 计算空气动力研究所，四川 绵阳 621000)

摘要： 高阶精度加权紧致非线性格式(WCNS)越来越广泛地应用于复杂流动数值模拟.WCNS 可以与多种无粘通量分裂方法结合起来使用.但是,常见的通量分裂方法都是基于低阶格式发展起来的,目前还不清楚哪些通量分裂方法最适合 WCNS,也不知道这些方法与高阶格式结合时将会产生什么效果.表面热流计算是高超声速流动数值模拟的难点之一,为了在热流计算时选择合适的通量,研究了多种通量分裂方法的耗散大小.每种通量都可以表示成中心部分与耗散部分之和.这些通量的中心部分相同且非常简单,但是耗散部分较为复杂,且不同的通量分裂方法可导致不同的耗散表达式.通过对通量耗散进行分析可以发现耗散大小与网格界面两侧的物理量跳跃近似线性正相关.数值计算表明高阶格式得到的网格界面左右两侧的物理量跳跃通常远比低阶格式小,因而带来的通量耗散小.通过 3 个典型算例考察了通量耗散对热流计算的影响,其中包括高超激波/边界层干扰算例.基于对 van Leer 通量、Steger-Warming 通量、KFVS 通量、Roe 通量、AUSM 类通量和 HLL 类通量的考察,给出了通量选择建议.

关 键 词： 加权紧致非线性格式； 激波/边界层干扰； Euler 通量； 高阶精度； 热流

引用本文/Cite this paper：

TU Guo-hua, CHEN Jian-qiang, MAO Mei-liang, ZHAO Xiao-hui, LIU Hua-yong. On the splitting methods of inviscid fluxes for implementing high-order weighted compact nonlinear schemes[J]. *Applied Mathematics and Mechanics*, 2016, **37**(12)：1324-1344.

涂国华，陈坚强，毛枚良，赵晓慧，刘化勇. 关于高阶精度 WCNS 格式的无粘通量分裂方法[J]. 应用数学和力学，2016，**37**(12)：1324-1344.